Alluvial record of an early Eocene hyperthermal within the Castissent Formation, Pyrenees, Spain

Louis Honegger[1], Thierry Adatte[2], Jorge E. Spangenberg[3], Jeremy K. Caves Rugenstein[4], Miquel Poyatos-Moré[5], Cai Puigdefabregas[6], Emmanuelle Chanvry[7], Julian Clark[8], Andrea Fildani[8], Eric Verrechia[2], Kalin Kouzmanov[1], Matthieu Harlaux[1], Sébastien Castelltort[1]

[1]Department of Earth Sciences, University of Geneva, Rue des Maraîchers 13, 1205 Geneva, Switzerland
[2]Institut of Earth Sciences, Géopolis, University of Lausanne, 1015 Lausanne, Switzerland
[3]Institute of Earth Surface Dynamics (IDYST), Géopolis, University of Lausanne, 1015 Lausanne, Switzerland
[4]Max Planck Institute for Meteorology, Bundesstraße 53 20146, Hamburg, Germany
[5]Department of Geosciences, University of Oslo, Sem Sælands vei 1, 0371 Oslo, Norway
[6]Department of Earth and Ocean Dynamics, University of Barcelona, C/ Martí i Franquès, s/n, 08028 Barcelona, Spain
[7]University of Poitiers & CNRS, IC2MP, INC, 86000 Poitiers, France
[8]Equinor Research Center, 6300 Bridge Point Parkway, Building 2, Suite 100, Austin, Texas, USA

Correspondence to: Louis Honegger (*louis.honegger@unige.ch*)

Abstract. The late Palaeocene to the middle Eocene (57.5 to 46.5 Ma) recorded a total of 39 hyperthermals—periods of rapid global warming documented by prominent negative carbon isotope excursions (CIEs) as well as peaks in iron content—have been recognized in marine cores. Documenting how the Earth system responded to rapid climatic shifts during hyperthermals provides fundamental information to constrain climatic models. However, while hyperthermals have been well documented in the marine sedimentary record, only a few have been recognized and described in continental deposits, thereby limiting our ability to understand the effect and record of global warming on terrestrial systems. Hyperthermals in the continental record could be a powerful correlation tool to help connect marine and continental deposits, addressing issues of environmental signal propagation from land to sea. In this study, we generate new stable carbon isotope data (δ^{13}C values) across the well-exposed and time-constrained fluvial sedimentary succession of the early Eocene Castissent Formation in the South-Central Pyrenees (Spain). The δ^{13}C values of pedogenic carbonate reveal—similarly to the global records—stepped CIEs, culminating in a minimum δ^{13}C value that we correlate with the hyperthermal event "U" at *ca.* 50 Ma. This general trend towards more negative values is most probably linked to higher primary productivity leading to an overall higher respiration of soil organic matter during these climatic events. The relative enrichment in immobile elements (Zr, Ti, Al) and higher estimates of mean annual precipitation together with the occurrence of small iron-oxide/hydroxide- nodules during the CIEs suggest intensification of chemical weathering and/or longer exposure of soils in a highly seasonal climate. The results show that even relatively small-scale hyperthermals compared with their prominent counterparts, such as PETM, ETM2 and 3, can leave a recognizable signature in the terrestrial stratigraphic record, providing insights into the dynamics of the carbon cycle in continental environments during these events.

1 Introduction

From the end of the Palaeocene, a period of global warming reached its climax during the Early Eocene Climatic Optimum (EECO) (Westerhold and Röhl, 2009; Hyland and Sheldon, 2013). The EECO started *ca.* 53 Ma ago and lasted until *ca.* 49 Ma ago (Westerhold et al., 2018), after which the climate began to cool (~Eocene-Oligocene transition, Zachos et al., 2001, 2008). Superimposed on, and coeval to, this globally warm epoch, brief periods of pronounced global warming known as "hyperthermals" standout as anomalies outside of background climate variability (Kirtland-Turner et al., 2014; Dunkley Jones et al., 2018). The Palaeocene-Eocene Thermal Maximum (PETM; ~56 Ma) was the first of these events to be identified globally because of its exceptional magnitude and preservation in both marine and continental deposits (Koch et al., 1992). To date, for the late Palaeocene – early Eocene period, a total of 39 hyperthermal events of lesser magnitude have been identified from marine cores (Lourens et al., 2005; Sexton et al., 2011; Kirtland-Turner et al., 2014; Lauretano et al., 2015, 2016; Westerhold et al., 2018), among which the most prominent and studied are the Eocene Thermal Maximum (ETM) 2 and 3, H2, and I1 and I2 events (Cramer et al., 2003; Lourens et al., 2005; Nicolo et al., 2007; Lunt et al., 2011; Deconto et al., 2012; Kirtland-Turner et al., 2014; Lauretano et al., 2016; Westerhold et al., 2017) (Fig. 1). In the marine stratigraphic record, these events are primarily characterized by paired negative excursion in carbon and oxygen isotope data exceeding background variability (Cramer et al., 2003; Nicolo et al., 2007; Zachos et al., 2008; Sluijs and Dickens, 2012; Lauretano et al., 2016), i.e. typically with amplitude greater than the standard deviation (SD) of pre-hyperthermal background values.

In deep marine settings, the carbon isotope excursions (CIE) are typically paired with an increase in iron concentration and decrease in carbonate content, indicating ocean acidification potentially linked with high atmospheric CO_2 concentrations (Nicolo et al., 2007; Slotnick et al., 2012; Westerhold et al., 2018). In coastal marine sections, early Eocene hyperthermal events are generally associated with an enhanced flux of terrigenous material, interpreted as linked to accelerated hydrological cycle and higher seasonality (Schmitz et al., 2001; Bowen et al., 2004; Nicolo et al., 2007; Slotnick et al., 2012; Payros et al., 2015; Dunkley Jones et al., 2018), although several studies document a spatially heterogeneous hydrological climatic response during the PETM (Bolle and Adatte, 2001; Kraus and Riggins, 2007; Giusberti et al., 2016; Carmichael et al., 2017). In fluvial systems, the abrupt warming of the PETM was found to be associated with expansion and coarsening of alluvial facies combined with an increase of the magnitude of flood discharge (Foreman et al., 2012; Pujalte et al., 2015; Chen et al., 2018), as well as enhanced pedogenesis (Abels et al., 2012). Yet, how continental systems reacted to the other, smaller-magnitude hyperthermals of the early Eocene remains to be documented. In particular, because of the subaerial nature and lateral preservation dynamics of alluvial systems (e.g., Foreman and Straub, 2017; Straub and Foreman, 2018), the extent to which fluvial successions can provide complete and faithful archives of past climatic events, especially those with the smallest magnitudes, is still largely unknown (Foreman and Straub, 2017; Trampush et al., 2017; Straub and Foreman, 2018). Addressing this question is particularly critical for studies focussing on environmental signal propagation in source-to-sink systems (e.g., Castelltort and Van Den Driessche, 2003; Duller et al., 2019; Romans et al., 2016; Schlunegger and Castelltort, 2016), which require high-resolution continental-marine correlations such as those provided by the PETM (e.g., Duller et al., 2019) or by other hyperthermals of the early Eocene.

To address these issues, we explored the geochemical signature (carbon and oxygen stable isotopes, major and trace elements) and the sedimentology of the fluvial deposits of the Ypresian age Castissent Fm. (South-Central

Pyrenees, Spain, Fig. 2). First, we generated a new carbon isotope profile from a paleosol succession rich in carbonate nodules across the Castissent Fm. in order to compare these results with a global $\delta^{13}C$ record. The data suggest that this fluvial succession preserves a record of hyperthermal "U" event at *ca.* 50 Ma, providing important constraints to its depositional the age. Second, we used the major and trace element composition of bulk floodplain material in order to explore the climatic impact of such hyperthermal, including empirical reconstructions of mean annual precipitation, allowing us to discuss soil dynamics during global warming. This study identifies for the first time in a continental succession an event so far only recorded in marine sediments, thereby demonstrating the global breadth of these climatic events and the complementarity of oceanographic and terrestrial archives.

2 Geological setting

The Castissent Formation comprises fluvial deposit of Ypresian age cropping out in the Tremp-Graus Basin (South-Pyrenean foreland basin, Marzo et al., 1988, Fig. 2). The Castissent Fm. is defined by its prominent overall sand-rich character, and is composed by three coarse-grained channels complexes (labelled as Members A, B and C) separated by four marine incursions (M0 to M3) inferred from the observation of marginal coastal bioclast-rich horizons developed up into the upper deltaic plain and correlative with finer dark-grey mudstones and calcretes in the fluvial segment of the Castissent (Marzo et al., 1988). This major fluvial progradation is correlated westwards with deep-water turbidite sequences of the Arro and Fosado Formations in the Ainsa Basin (Fig. 3, Mutti et al., 1988; Nijman and Nio, 1975; Nijman and Puigdefabregas, 1978; Pickering and Bayliss, 2009). In the upstream, eastern counterparts of the Castissent Fm., the channel complexes are intercalated with yellow to red coloured paleosols. Sub-spherical to slightly elongated carbonate nodules with a diameter ranging from 1 mm to 4 cm are omnipresent in the paleosols (Fig. S1). Studies of the Castissent Fm. tentatively attributed its occurrence to an important pulse of exhumation and thrust activity in the hinterland at *ca.* 50 Ma, in possible combination with a late-Ypresian sea-level fall (Puigdefabregas et al., 1986; Marzo et al., 1988; Whitchurch et al., 2011; Castelltort et al., 2017), both resulting in reduced available accommodation space enhancing progradation and amalgamation (Chanvry et al., 2018).

The Chiriveta section, encompassing the Castissent Fm., is situated in a continental paleogeographic position prone to pedogenesis and slightly off-axis from the more "in-axis" amalgamated sand-rich type section of Mas de Faro (Fig. 2); for paleo-position and correlation see also Figs. 10 and 12 in Marzo et al. (1988).

In the Chiriveta location, stratigraphic constraints are limited to the identification of European Mammals zone MP10 (Badiola et al., 2009), which provides an age range of 50.73 to 47.4 Ma (GTS2012). This age span is refined by bio- and magnetostratigraphic data from the Castissent Fm. outcrops of the Campo location, about 40 km further west (Kapellos and Schaub, 1973; Tosquella, 1995; Bentham and Burbank, 1996; Tosquella et al., 1998; Payros et al., 2009) (fig. 3). Because of its outcropping extent, the Castissent Fm. has been mapped from west to east across these sections (Nijman and Nio, 1975; Nijman, 1998; Poyatos-Moré, 2014; Chanvry et al., 2018). The low slope of the Castissent Fm. (*ca.* 2.3×10^{-4} m/m, see supplementary Table S1) indicate an elevation drop of *ca.* 1 m between the Chiriveta section and the Campo section. Given an average flow depths of 3.75 m in the Castissent channels based on measurement in the Chiriveta and La Roca sections, we thus assume no significant time-lag of deposition between both sections. In the Campo section, Kapellos and Schaub (1973) find the transition between the *D. lodoensis* and the *T. orthostylus* nannoplankton (NP) zones at *ca.* 200 m below the base of the Castissent Fm. and the transition between the *T. orthostylus* and the *D. sublodoensis* NP zones in the transgression *ca.* 100 m above the uppermost member of the Castissent Fm. This indicates that the Castissent Fm. was deposited during NP13. Magnetostratigraphic data of the same section by Bentham and Burbank (1996) place the transition between the C22r and C22n magnetozones closely above the top of the Castissent Fm. We thus used the recent astrochronologic age models of Westerhold et al. (2017), which obtain numerical ages of 50.777±0.01 and 49.695±0.043 Ma respectively for the base and top of C22r, and obtain a numerical age of 50.534±0.025 Ma for the base of NP13 based on ODP site 1263. Considering the data available and their resolution, we suggest a depositional age span between 50.5 and 49.7 Ma for the Castissent Fm. (reported in green on Fig. 1). According to global isotopic records (Fig. 1), this period was marked by 4 hyperthermals labelled S/C22rH3, T/C22rH4, U/C22rH5 and V/C22nH1 (Cramer et al., 2003; Lauretano et al., 2016; Westerhold et al., 2017).

3 Material and methods

3.1 Sampling

A total of 74 samples were collected from the early-Eocene Chiriveta section for geochemical studies. All samples consist of floodplain material and were taken below the weathering depth (~50 cm), with an average resolution of 1 m. Resolution was increased by a factor of 2 in specific horizons such as red beds. When important sandbodies occurred, lateral equivalent floodplain material or intercalated paleosol horizons were sampled. Each sample was split in two aliquots, one for major and trace element analysis and the other for carbon and oxygen stable isotope analysis on pedogenic carbonate nodules. The carbonate nodules were extracted from the bulk paleosol material by sieving and then cleaned by repeated washes with deionized water in an ultrasound bath. From each cleaned nodules set, subsamples of 1 to 4 nodules were taken, leading to a total of 149 sub-samples of pedogenic carbonate nodules.

3.2 Carbon and oxygen stable isotopes

Pedogenic carbonate nodules were crushed and powdered in an agate mortar and analysed for stable carbon and oxygen isotope composition at the Institute of Earth Surface Dynamics of the University of Lausanne (Switzerland) using a Thermo Fisher Scientific (Bremen, Germany) carbonate-preparation device and Gas Bench II connected to a Thermo Fisher Delta Plus XL isotope ratio mass spectrometer. The carbon and oxygen isotope compositions are reported in the delta (δ) notation as the per mil (‰) isotope ratio variations relative to the Vienna Pee Dee Belemnite standard (VPDB). The analytical reproducibility estimated from replicate analyses of the international calcite standard NBS-19 and the laboratory standard Carrara Marble was better than ± 0.05 ‰ (1 sigma) for $\delta^{13}C$ and ± 0.1 ‰ (1 sigma) for $\delta^{18}O$.

3.3 Major and trace element composition

Fifty-two bulk paleosol samples were analysed for major and trace elements using X-ray fluorescence (XRF) spectrometry. Crushed bulk powders (<80 μm) were mounted in a plastic cup covered by a thin polypropylene film (4 μm-thick) and analysed in the laboratory with a Thermo Niton XL3t® portable XRF analyzer fixed on a test stand. Analyses were performed with a beam diameter of 8 mm, to determine the concentrations of 34 major and trace elements (from Mg to Au). Each measurement took 120 s, consisting of two 60 s cycles on four different filters (15 seconds on low, main, high, and light ranges), operating the X-ray tube at different voltage to optimize the fluorescence and peak/background ratios of the different elements. The limits of detection were of 10's ppm for most elements, except for Mg, Si, and Al which are at wt% level. Sodium is too light to be detected. The acquired spectra were transferred to a computer using NDT software version 8.2.1. (Thermo Fisher Scientific, Waltham, Ma, USA). The same material has been analysed for twenty-three major and trace elements on fused and pressed discs, respectively, using a PANalytical PW2400 XRF spectrometer with copper (Cu) tube at the University of Lausanne to cross-calibrate the compositions measured with the Niton XL3t® portable XRF analyzer.

3.4 Mean annual precipitation

The mean annual precipitation estimate (MAP) used in this study was estimated from the empirical relationship between MAP and CaO/Al_2O_3 ratio for Mollisols from a national survey of North American soils according to the following equation: MAP (mm) = $-130.9 \times \ln(CaO/Al_2O_3) + 467$ (Sheldon et al., 2002). CaO and Al_2O_3 concentrations were measured on bulk paleosol material. Climate linked to the MAP estimate was classified based on the following boundaries: arid to semiarid at 250 mm and semiarid to subhumid at 500 mm (Bull, 1991).

3.5 Grain-size estimation

The relative grain-size variation of the sediment samples was estimated from their major element compositions. Si, Ti and Zr are more concentrated in the coarse fraction of the sediment as they are found in larger mineral grains, whereas Al is more concentrated in the finer fraction of the sediment because is mostly linked to clay minerals (Lupker et al., 2011, 2012; Croudace and Rothwell, 2015). Grain size variation throughout the section was estimated using Si/Al, Ti/Al and Zr/Al ratios, therefore, an increase in these ratios suggests a relative increase in the proportion of coarser material in the sample.

3.6 Correlation with target curves

The measured $\delta^{13}C$ dataset was compared with a time-equivalent ODP 1263 global $\delta^{13}C$ record reported by Westerhold et al. (2017) using the Analyseries software (Paillard et al., 1996). The $\delta^{13}C$ record of site 1263 was favoured over those of ODP 1209 and 1258 covering the Castissent Fm. time-period, because it is continuous and has a higher resolution. Correlations between the $\delta^{13}C$ record of site 1263 and the $\delta^{13}C$ record of the Chiriveta section were performed in order to optimize the Pearson correlation coefficient (r) and by minimizing abrupt variations in sedimentation rates. Well-defined peaks in both $\delta^{13}C$ records were used as tie-points for the correlation and the number of tie-points was kept minimum (<10) so as not to force the correlations.

4 Results

4.1 Sedimentology of the Castissent Formation at Chiriveta

We here describe the section logged and sampled in this work (Fig. 4). At Chiriveta, the Castissent Fm. is a paleosol-rich succession, which shows greyish-yellow to red-brown mottled floodplain paleosols (Fig. 4A-B), corresponding laterally to thick, medium to coarse-grained quartz-rich channel-fill deposits (width/depth ratio = 20-50; Marzo et al. (1988)) and over-bank deposits flowing parallel to the main structures of the growing Pyrenean orogeny (Marzo et al., 1988). At the base of the section, the first marine incursion M0 is situated at the top of a 20 m-thick coarse-grained tidal bar deposit with herringbone cross-stratifications and oyster shells (Fig. 4C). In the Chiriveta section, the Castissent Member A is a 48 m-thick interval comprising two main medium-grained sandbodies of light coloration of 5.40 and 1.5 m in thickness respectively. Bedforms observed in the first sandbody have a mean height of 24 cm (*n* = 9). The second marine incursion M1 is located at 48 m just below the Castissent B Member and consists of a 2 m-thick grey interval interpreted by Marzo et al. (1988) brackish-lagoonal water facies (Fig. 4B-F). The Castissent B Member (Fig. 4G) is a 12 m-thick and laterally-extensive (width/depth ratio ≥ 250; Marzo et al. (1988)) amalgamated sandbody with a micro-conglomeratic erosive base. Grain size is overall larger than in Member A, and ranges from fine sand to large pebbles. Sandbody tops show a fining-upward trend and are capped by mottled siltstone packages. Mottled siltstone layers are interpreted as pedogenized over-bank deposits based on roots traces and their capping relationship with underlying sandbody deposits (observed at 26 m, 76 m, 89 m and 96 m in Fig. 4, Fig. 4H). More regular and sheet-like sandbodies interbedded with mottled siltstone layers are observed upwards. The section ends with a 23 m-thick, medium to very coarse tidally-influenced sandstone deposit interpreted as the equivalent M3 marine incursion by Marzo et al. (1988). Although Castissent Member C was not interpreted by Marzo et al. (1988) in this section, a 2m-thick fine-grained sandbody at ca 80 meters in our section could be the condensed lateral equivalent of it (Fig. 5)

4.2 Stable isotopic record

Carbon and oxygen isotope ratios from the carbonate nodules are presented in Fig. 5. The δ^{13}C values vary between -10.9 and -1.9‰ with a mean value and 1 SD of –7.7 ± 1.6 ‰. Six CIEs (named A to F in Fig. 5 and colour coded in Fig. 6) are more negative than -9.3‰ (i.e., the mean value – 1 standard deviation) amongst which one (CIE D) is below 2 SDs. The values are –9.6, –9.8, –9.9, –10.9, –9.9 and –9.4‰ for CIEs A to F respectively. At the bottom of the section, CIE A is followed by a relatively constant interval of mean δ^{13}C values. CIE B, situated in the first red bed, marks the beginning of a stepped δ^{13}C trend (around ±1 SD) leading to the minimum CIE D. The second part of the section shows two more CIEs separated by the highest δ^{13}C value at 74 m. CIE F is the least prominent of all CIEs. The δ^{18}O values vary between –7.0 and –5.0‰ with a mean value of –6.0 ± 0.4 ‰, which makes them less dispersed than the δ^{13}C record. Nine negative oxygen isotope excursions are more negative than the mean value – 1 SD, amongst which one is below 2 SD reaching a minimum value of –6.8‰ at 19 m. The oxygen isotope excursions do not correspond with CIEs described above.

4.3 Major and trace elements

Titanium (Ti), Aluminium (Al) and Zirconium (Zr) concentrations measured on bulk paleosols are plotted in Figure 5. These elements are commonly considered as immobile and are expected to concentrate in more weathered soils. Ti values vary between 0.18 and 0.52% with a mean value of 0.34% and a standard deviation of 0.08. Al values vary between 3.03 and 9.35% with a mean value of 5.85% and a standard deviation of 1.53. Zr values vary between 67 and 204 ppm with a mean value of 128 ppm and a standard deviation of 35. Mean annual precipitation (MAP) estimates values vary between 185 and 754 mm/y with a mean value of 376 mm/y and a standard deviation of 111. Ti, Al, Zr and MAP show a similar trend starting from the base of the section with a global increase of all values toward CIE C and a decrease afterwards. All CIEs show higher value of Ti, Al, Zr and MAP except CIE F. Based on Bull (1991), an average value of 387 mm/y for the MAP in the Chiriveta section represent a semi-arid climate (Fig. 5). All CIEs show an increase in MAP.

5 Discussion

5.1 Carbon and oxygen isotopic record

5.1.1 Identifying the CIE

In continental successions, the carbon isotope composition of pedogenic carbonate nodules—which consists of calcareous concretions between 1 mm and 4 cm diameter formed *in situ* in the floodplain—have been shown to be sensitive to environmental conditions during their formation (e.g., Millière et al., 2011a, 2011b), and are therefore a promising tool to track how environments respond to carbon cycle perturbation . The carbon isotope composition of the soil carbonate nodules depend on the δ^{13}C value of the atmospheric CO_2 and soil CO_2, which in turn is a function of the δ^{13}C of the atmospheric CO_2 and the overlying plants, as well as the soil respiration flux and the partial pressure of atmospheric CO_2 (Cerling, 1984; Bowen et al., 2004; Abels et al., 2012; Caves et al., 2016).

The δ^{13}C vs δ^{18}O diagram for the pedogenic carbonate nodules from the Chiriveta section (r = -0.26, n = 149) suggests a good preservation of the primary isotopic signal (Figure 6), with an average value of δ^{13}C = –7.7 ± 1.6 ‰ similar to mid-latitude late-Palaeocene to Eocene continental δ^{13}C values (excluding the PETM samples) observed elsewhere (e.g., McInerney and Wing, 2011; and references therein), and a spread comparable with δ^{13}C values from carbonate nodule analysed for the same period in the Bighorn Basin (Bowen et al., 2001). Fig. 6 emphasizes that early-Eocene carbonate nodules display overall more negative δ^{13}C values than the Holocene nodules, which is consistent with a large compilation of data from eastern Eurasia (Caves Rugenstein and Chamberlain, 2018). Pre-PETM δ^{18}O values from carbonate nodules from the same area (–4.5 ± 0.4 ‰) (Hunger, 2018) show similar values than the Chiriveta section's measurements (–6.0 ± 0.4 ‰). Oxygen and carbon isotopes are not coupled during hyperthermal events in continental record as already observed by Schmitz and Pujalte, (2003), Bowen et al., (2001) for the PETM isotopic excursion. Though the precise mechanisms that produce stable δ^{18}O during CIE are still debated, mid-latitude precipitation δ^{18}O appears to be relatively insensitive to changes in atmospheric pCO_2 and warming, particularly in greenhouse climates (Winnick et al., 2015). In contrast, the stable δ^{18}O values of soil carbonates from the Pyrenean foreland basin (–5.5 ± 0.9 ‰) is likely additionally stabilized by its position close to the coast (Cerling, 1984; Kukla et al., 2019) compared for example to those of the Bighorn Basin (–9.0 ± 0.6 ‰). This is in line with a more continental paleogeographical position of the Bighorn Basin compared to the Tremp-Graus Basin at the time (Seeland, 1998).

A hyperthermal event recorded in marine sediments is defined by a paired negative carbon and oxygen stable isotope excursions that are more negative than the mean value minus 1 SD (Kirtland-Turner et al., 2014). This definition may not be applicable to continental deposits, because continental systems respond differently than marine systems to the carbon cycle perturbations. Though the marine δ^{13}C record is thought to record the global CO_2 δ^{13}C, the δ^{13}C value of the marine dissolved inorganic carbon is also influenced by dissolution of carbonates at depth (McInerney and Wing, 2011). In contrast, δ^{13}C in pedogenic nodules varies with soil properties, atmospheric and soil pCO_2 and δ^{13}C, and the rate and nature of carbon input and/or output by soil respiration (Bowen et al., 2004; Sheldon and Tabor, 2009). These processes create complexities in estimating CIEs in soil carbonate nodules and in marine carbonates (McInerney and Wing, 2011). Nevertheless, we used Turner et al. (2014)'s hyperthermal definition as a starting point to filter the high-resolution variations in the Chiriveta section. We identify 16 samples with CIE values more negative than the mean –1 SD. Among these 16 samples, we recognized 6 discrete CIEs (named A – F in Fig. 5 and 7). Both marine incursion M1 and M2 show an abrupt shift from –9 to –10‰ in continental δ^{13}C values towards more (positive) marine values of –4 to –2‰; this point to a progressive higher contribution of seawater to the formation of the carbonate nodules.

Six correlation options with the global record were explored in the time-window of the Castissent Fm. (Figure S2 and S3 in the Supplement). The correlation presented in Figure 7A was favoured as it shows: i) reasonable sedimentation rates variations, ii) a similar amplitude to the CIE in the global record, and iii) the highest correlation coefficient (r = 0.65, n = 71). Moreover, it plots on the same trend regarding hyperthermal CIE amplitudes in marine and continental environments suggesting a common mechanism of global climatic change with events I1, I2, H2 and ETM2 (Figure 7B). Based on these observations and obtained correlation, we suggest that only hyperthermal U is preserved in the Chiriveta section and that it is correlated with CIE D. Sedimentation rate obtained with the favoured correlation (Figure 7) varies between 0.1-0.29 mm/y, consistent with sedimentation rates reported for other Eocene floodplain successions (Kraus and Aslan, 1993). The correlation coefficient of r = 0.65 suggests an overall good signal preservation in the studied continental section for a 40 kys climatic event.

5.1.2 Mechanisms causing the CIE

An increase in temperature could potentially release significant amount of CO_2 into the atmosphere (Trumbore et al., 1996; Melillo et al., 2014). The amplitude and duration of Eocene CIEs are approximately 30% of the one recorded for the PETM, we hypothesize that the climatic effects of smaller-scale hyperthermals can be linearly scaled to the PETM. Based on this assumption and in order to get a rough approximation without considering a non-linear sensitivity response, a smaller-scale hyperthermal would imply a release of approximately 500 to 1500 Gt of carbon to the ocean and atmosphere reservoir and a global temperature rise of about 1.5–2.5°C. This estimation correspond to the 1500 – 4500 Gt of carbon released during the PETM, causing a rise of 5–8°C (Bowen et al., 2006), and is in line with previous estimations of ~3 and ~2°C warming for ETM2/H1 and H2 events respectively (Stap et al., 2010). A release of 500 to 1500 Gt of carbon in the form of methane would imply a marine CIE of 0.8 to 2.3‰ or 0.3 to 0.9‰ if the carbon origin is dissolved organic carbon (DOC) (Sexton et al., 2011). The latter seems more plausible regarding the observed amplitude of ~1‰ measured in the marine record for hyperthermal U (Westerhold et al., 2017) and the supposed origin linked to the oxygenation of deep-marine DOC of post-PETM hyperthermals (Sexton et al., 2011). A global shift of -1‰ in δ^{13}C can however not fully explain the 3‰ shift in δ^{13}C observed in this study.

The δ^{13}C mean value in the Chiriveta section is –7.7 ± 1.6 ‰. This value reflects an overall equilibrium with a mean atmospheric CO_2 of –7‰ (Koch et al., 1995) and is coherent with pre-PETM δ^{13}C values of –7.1 ± 0.9 ‰ found in the same area (Hunger, 2018; Fig. 6). It is possible to calculate from the (small-scale) hyperthermal δ^{13}C excursions in the marine environment the shift to be expected in soil carbonate nodules by using known fractionation coefficients (Koch et al., 1995, 2003); the expected δ^{13}C value in carbonate nodules, only considering the respiration of organic matter, is–11‰ (Fig. 8). This value is within the range of those measured from the Chiriveta section, where some nodules reach values as low as -10.9‰. We suggest that the bacterial respiration of organic matter, enhanced by warmer temperatures (e.g.; Davidson and Janssens, 2006; Trumbore et al., 2006), may also have contributed to the lower δ^{13}C values of nodules during the CIEs (Fig. 8). On geological timescales, soil organic carbon can be considered at steady state with equal organic carbon inputs and outputs from the soil (Koven et al., 2017). Respiration (carbon output after mineralization as CO_2) is thought to be more sensitive to global warming than gross primary productivity (organic carbon input as organic matter) leading to a depletion of the total soil carbon pool with time during transient global warming events; although the precise sensitivity of gross primary productivity remains poorly constrained (Davidson and Janssens, 2006). Large uncertainties remain about carbon dynamics and their timescale in the soils during climate changes. Parameters such as the vegetation type (Klemmedson, 1989), temperatures (Koven et al., 2017), soil geochemistry (Torn et al., 1997; Doetterl et al., 2015), and soil water content (Davidson et al., 2000) have been shown to be important controlling factors within historical timescales.

Considering these caveats, we estimate the maximum possible contribution of enhanced soil carbon respiration to negative $\delta^{13}C$ excursions during the CIEs. Using typical values for the organic carbon reservoir comprising fast and slow cycling carbon in soils in arid to semi-arid ecosystems of 5.6–19.2 kgC/m^2 (Klemmedson, 1989; Raich and Schlesinger, 1992), respiration fluxes starting at a steady state value of 0.5 kgC/yr, and a respiration rate sensitivity *ca.* 5%/degree (Raich and Schlesinger, 1992) (Q_{10} = 1.5), we estimate that all of the organic carbon in soils would be consumed within 250 to 850 yrs., given an increase of 1°C and without changing the carbon input rate. Though there are a number of assumptions in this first-order estimate, the timescale of soil carbon depletion is substantially shorter than our estimate of the timescale of the CIE (~36 kyrs) (Fig. 7). As evidenced by this calculation, an increase in soil respiration triggered by warmer temperatures cannot be the sole mechanism driving the CIE shift over multi-millennial time-scales. Instead, we suggest that during these transient warmings, this mechanism is associated with a high primary productivity—resulting in a greater input of carbon to the soil—leading to an overall higher soil respiration of organic matter. Coupled with lower atmospheric $\delta^{13}C$ during hyperthermals, this mechanism caused a pronounced CIE in soil carbonate nodules.

5.2 Geochemical signature of hyperthermal events

Major and trace elements compositions of floodplain sediments is a function of river dynamics, climate, and sediment grain-size (Lupker et al., 2012; Turner et al., 2015). Based on the CIEs, we defined six intervals showing a relative enrichment (up 10 to 30% compared to the average value) in immobile elements such as Ti, Al and Zr (Fig. 5). To ensure that major and trace concentrations are not grain-size biased, we plotted grain-size proxies Si/Al, Ti/Al and Zr/Al (Lupker et al., 2012; Turner et al., 2015), which all exhibit a relatively stable trend, not connected with the immobile element concentrations (Figure S4 in the Supplement). The enrichments in Ti, Al and Zr suggest mature paleosols with potential intense weathering due to enhanced humid climatic conditions; but may also correspond to a longer exposure time on a stable floodplain, allowing leaching of mobile elements and relative enrichment of immobile elements (Sheldon and Tabor, 2009). Pedogenic nodules are frequent in well-drained soil profiles associated with a climate regime where the potential evapotranspiration is greater than the mean annual precipitation rate (Slessarev et al., 2016) and with a mean annual precipitation < 800 mm/year (Cerling, 1984; Retallack, 1994; Sheldon and Tabor, 2009). These conditions correspond to climate ranging from arid to sub-humid conditions (Hasiotis, 2004; Prochnow et al., 2006; Hyland and Sheldon, 2013). This agrees with MAP values obtained for the paleo-precipitation estimate (Fig. 5) and with a smectite/kaolinite >1 assemblage dominating some of the studied soils (Nicolaides, 2017, Table S2 in the Supplement); all suggestive of a semi-arid to sub-humid climate with seasonal humidity (Arostegi et al., 2011). Associated with CIEs C and D in red bed deposits, sub-milimetric iron-oxide and hydroxides nodules made of concentric hematite and goethite were found together with carbonate nodules (Fig. S1). This suggest a seasonal climate as hematite forms under more arid soil condition than goethite (Kraus and Riggins, 2007). Together, these observations are in line with an acceleration of the hydrological cycle and a higher seasonality, as has been observed during the PETM, H1, H2; I1 and I2 hyperthermals (Bowen et al., 2004; Nicolo et al., 2007; Slotnick et al., 2012; Dunkley Jones et al., 2018). Therefore, combined with CIEs, we suggest that small scale hyperthermals in continental records can be recognized by an increase in the weathering index (Hessler et al., 2017) and by an increase in the immobile element concentrations, both related to an increase in precipitation intensity.

5.3 High-resolution hyperthermal signal

The high-resolution isotopic and elemental record of the Chiriveta profile allow us to highlight the dynamics and variability of a hyperthermal event. We do not observe a unique peak in δ^{13}C, but rather a stepped isotopic signal suggesting, together with above-discussed geochemical data, a climatic oscillation alternating with variably intense precipitations and leaching conditions during a climax spanning *ca.* 150 kyrs (interval CIE B to D). Such a climatic behaviour, was already described for the PETM, during the pre-onset excursion (Bowen et al., 2015) and in the core CIE of the PETM (Giusberti et al., 2016). Moreover, the δ^{13}C climax (CIE D) does not correspond to the highest concentrations of immobile elements nor maximum MAP estimates, which we estimate occur during CIE C, which predates by *ca.* 50 kyrs the CIE D (Fig. 7). The minimum δ^{13}C value therefore does not seem to be coeval with the most extreme climatic response, suggesting a complex environmental response. However, because sedimentation in floodplain depositional settings is a function of the channel position and flood frequency, the relative concentration of elements may reflects the changes in river dynamics instead of climatic variability, which could explain the mismatch between minimum values in CIE and the climatic response. More high-resolution hyperthermal studies in coeval continental sections are needed to better understand the relationships between proxies.

5.4 Possible implication for the preservation potential of hyperthermals in continental sections

Major events such as the PETM have proven to be detectable in both marine and continental environments (e.g.; Abels et al., 2016; Koch et al., 1992), but the signal and preservation potential of smaller scale climatic events (e.g. hyperthermal events L to W in Lauretano et al., 2016), may be more difficult to detect (Foreman and Straub, 2017) because of the inherent highly dynamic nature of sedimentation in fluvial deposits. To address this issue in the present case study, we calculated the compensation time scale (Tc) of the Castissent Fm. Tc is a time-scale characteristic of an alluvial basin below which stratigraphic signals with shorter durations may be of autogenic origin, thereby giving a scale below which allogenic forcing should be interpreted carefully (Wang et al., 2011; Foreman and Straub, 2017; Trampush et al., 2017). In other words, an external forcing signal with a duration smaller than Tc will be challenging to identify from background variability; the external forcing must be therefore of a duration longer than Tc and optimally twice Tc (Foreman and Straub, 2017). Tc max can be calculated by dividing the topographic roughness or maximum channel depth by the average subsidence or deposition rate (Wang et al., 2011). Using an average sedimentation rate of 0.17 mm/yr and an average channel depth of 3.75 m, we obtained a mean Tc of 22,000 yrs, which means that hyperthermal events of 40 kyrs duration (time-scale of hyperthermal U and preceding CIE) have the potential to be recorded despite fluvial system dynamics. Our estimate of preservation potential assumes steady sedimentation rates throughout the section. But, sedimentation in terrestrial records is not uniform (steady) but rather highly variable, resulting in spatial and temporal changes in facies and deposition rates ranging from < 0.1 to 1-2 mm/yr (Marriott and Wright, 1993; Bowen et al., 2015; Kraus et al., 2015). However, mean accumulation rates give a reasonable estimate approximating more realistic (i.e., variable) sedimentation rates as observed in the Bighorn Basin (Bowen et al., 2015).Additionally, we analyse the vertical movement of the nearby structures to evaluate their potential influence on disrupting deposition at Chiriveta during Castissent times. The Chiriveta section was deposited near or at the axis of the Tremp-Graus basin (Nijman, 1998), which is bounded by the Bóixols thrust in the north and the Montsec thrust in the south (Marzo et al., 1988). The Tremp-Graus basin is transported as a piggy-back basin on the Montsec thrust emerging at the time approximatively 4 km south of the studied section (Nijman, 1998). In the basin axis, subsidence is the highest with rates of 0.1 to 0.29 mm/yr (this study and Marzo et al., (1988)). Taking into account a vertical movement rate of the Montsec thrust of 0.03 to 0.1 mm/yr during the Castissent time-interval (based on a horizontal displacement of 7 km, a period of activity lasting 26 Ma and a thrust dip between 6° and 20° (Farrell et al., 1987; Nijman, 1998; Clevis et al., 2004; Whitchurch et al., 2011), we estimate that the vertical displacement is no more than equal to sedimentation rates in the basin axis. This is consistent with the general absence of growth strata in the basin axis, although growth strata can indeed be observed closer to the Montsec (Nijman, 1998).

The rates of accumulation, distance to the main structures, and characteristic compensation time scale, together suggest that hyperthermal events of *ca.* 40 kys duration can be recorded in the Castissent Fm. These results confirm that, despite its highly dynamic nature, fluvial sedimentation may contain valuable record of high-frequency events, even in active tectonic contexts.

6 Conclusions

A new high-resolution isotopic record from the paleosol-rich deposits at the Chiriveta section identified a prominent negative carbon isotope excursion (CIE) in continental settings. We suggest that the CIE recorded in fluvial succession of the early Eocene Castissent Formation is the "U" event, identified for the first time in continental deposits. This climatic event, reaches δ^{13}C values of 2 sigma (standard deviation) below the mean and is heralded and followed by several smaller-scale stepped CIEs, which are interpreted as moments of enhanced primary productivity, leading to an overall higher soil respiration. We show that all these CIEs are relatively enriched in immobile elements (i.e., Ti, Zr and Al) and display an increase in MAP estimates. These observations coupled with the presence of iron-oxide nodules on an overall weathered succession, suggest an increase in precipitation rates during these events. The data presented in this study suggest a period of *ca.* 150 kyrs of contrasted climate alternating average and above background weathering conditions. Finally, the results of this demonstrate the importance of hyperthermal events in continental successions as well as in the preservation potential of such deposits.

Acknowledgements. The authors would like to acknowledge the lifetime work of Josep Serra Kiel, whose research and scientific contributions in the Pyrenees have been fundamental to this work and much beyond. This study has benefited from scientific discussion and field work with M. Perret, A. Nowak, C. Läuchli, T. Hunger, J. Vernier, K. Thomson, M. Odlum, A. Le Cotonnec and T. Maeder. Work supported by an Augustin Lombard grant from the SPHN Society of Geneva. Field work was supported by an Equinor grant to SC.

Isotopic, majors and trace data and tie points used for correlation can be found in the supporting information (Table S3 and S4 in the Supplement)

Author contributions. LH led the field work, sampling, sample preparation, data interpretation and writing. TA contributed to field work, sampling, data interpretation, discussion and writing. JES performed stable isotope analysis, data interpretation and writing. JKCR interpreted the data and writing. MPM and EC contributed to fieldwork, sampling, discussion and writing. CP, JC and AF supervised the fieldwork, discussions and writing. EV led discussions on the paleosols. KK and MH performed the XRF analysis. SC supervised the project and writing.

The authors declare that they have no conflict of interest

References

Abels, H. A., Clyde, W. C., Gingerich, P. D., Hilgen, F. J., Fricke, H. C., Bowen, G. J. and Lourens, L. J.: Terrestrial carbon isotope excursions and biotic change during Palaeogene hyperthermals, Nat. Geosci., 5, 326–329, doi:10.1038/ngeo1427, 2012.

Abels, H. A., Lauretano, V., van Yperen, A. E., Hopman, T., Zachos, J. C., Lourens, L. J., Gingerich, P. D. and Bowen, G. J.: Environmental impact and magnitude of paleosol carbonate carbon isotope excursions marking five early Eocene hyperthermals in the Bighorn Basin, Wyoming, Clim. Past, 12, 1151–1163, doi:10.5194/cp-12-1151-2016, 2016.

Arostegi, J., Baceta, J. I., Pujalte, V. and Carracedo, M.: Late Cretaceous – Palaeocene mid-latitude climates: inferences from clay mineralogy of continental-coastal sequences (Tremp-Graus area, southern Pyrenees, N Spain), Clay Miner., 46, 105–126, doi:10.1180/claymin.2011.046.1.105, 2011.

Bentham, P. and Burbank, D. W.: Chronology of Eocene foreland basin evolution along the western oblique margin of the South-Central Pyrenees., Tert. Basins Spain. Stratigr. Rec. Crustal Kinematics. World Reg. Geol., 6, 144–152, 1996.

Bolle, M.-P. and Adatte, T.: Palaeocene- early Eocene climatic evolution in the Tethyan realm: clay mineral evidence, Clay Miner., 36, 249–261, doi:10.1180/000985501750177979, 2001.

Bowen, G. J., Koch, P. L., Gingerich, P. D., Norris, R. D., Bains, S. and Corfield, R. M.: Refined isotope stratigraphy across the continental Paleocene-Eocene boundary on Polecat Bench in the northern Bighorn Basin, Int. Conf. Clim. biota early Paleogene, Powell, WY, United States, July 3-8, 2001, 33, 73–88, 2001.

Bowen, G. J., Beerling, D. J., Koch, P. L., Zachos, J. C. and Quattlebaum, T.: A humid climate state during the Palaeocene / Eocene thermal maximum, Nature, 432, 495–499, doi:10.1038/nature03109.1., 2004.

Bowen, G. J., Bralower, T. J., Delaney, M. L., Dickens, G. R., Kelly, D. C., Koch, P. L., Kump, L. R., Meng, J., Sloan, L. C., Thomas, E., Wing, S. L. and Zachos, J. C.: Eocene hyperthermal event offers insight into greenhouse warming, Eos, Trans. Am. Geophys. Union, 87, 165, doi:10.1029/2006EO170002, 2006.

Bowen, G. J., Maibauer, B. J., Kraus, M. J., Röhl, U., Westerhold, T., Steimke, A., Gingerich, P. D., Wing, S. L. and Clyde, W. C.: Two massive, rapid releases of carbon during the onset of the Palaeocene–Eocene thermal maximum, Nat. Geosci., 8, 44–47, doi:10.1038/ngeo2316, 2015.

Bull, W. B.: Geomorphic Responses to Climate Change: New York., 1991.

Carmichael, M. J., Inglis, G. N., Badger, M. P. S., Naafs, B. D. A., Behrooz, L., Remmelzwaal, S., Monteiro, F. M., Rohrssen, M., Farnsworth, A., Buss, H. L., Dickson, A. J., Valdes, P. J., Lunt, D. J. and Pancost, R. D.: Hydrological and associated biogeochemical consequences of rapid global warming during the Paleocene-Eocene Thermal Maximum, Glob. Planet. Change, 157, 114–138, doi:10.1016/j.gloplacha.2017.07.014, 2017.

Castelltort, S. and Van Den Driessche, J.: How plausible are high-frequency sediment supply-driven cycles in the stratigraphic record?, Sediment. Geol., 157, 3–13, doi:10.1016/S0037-0738(03)00066-6, 2003.

Castelltort, S., Honegger, L., Adatte, T., Clark, J. D., Puigdefàbregas, C., Spangenberg, J. E., Dykstra, M. L. and Fildani, A.: Detecting eustatic and tectonic signals with carbon isotopes in deep-marine strata, Eocene Ainsa Basin, Spanish Pyrenees, Geology, 45, 707–710, doi:10.1130/G39068.1, 2017.

Caves, J. K., Moragne, D. Y., Ibarra, D. E., Bayshashov, B. U., Gao, Y., Jones, M. M., Zhamangara, A., Arzhannikova, A. V., Arzhannikov, S. G. and Chamberlain, C. P.: The Neogene de-greening of Central Asia, Geology, 44, 887–890, doi:10.1130/G38267.1, 2016.

Caves Rugenstein, J. K. and Chamberlain, C. P.: The evolution of hydroclimate in Asia over the Cenozoic: A stable-isotope perspective, Earth-Science Rev., 185, 1129–1156, doi:10.1016/j.earscirev.2018.09.003, 2018.

Cerling, T. E.: The stable isotopic composition of modern soil carbonate and its relation to climate, Earth Planet. Sci. Lett., 71, 229-240., 1984.

Cerling, T. E. and Quade, J.: Stable Carbon and Oxygen Isotopes in Soil Carbonates, Clim. Chang. Cont. Isot. Rec., 217–231, doi:10.1029/GM078p0217, 1993.

Chanvry, E., Deschamps, R., Joseph, P., Puigdefàbregas, C., Poyatos-Moré, M., Serra-Kiel, J., Garcia, D. and Teinturier, S.: The influence of intrabasinal tectonics in the stratigraphic evolution of piggyback basin fills: Towards a model from the Tremp-Graus-Ainsa Basin (South-Pyrenean Zone, Spain), Sediment. Geol., 377, 34–62, doi:10.1016/j.sedgeo.2018.09.007, 2018.

Chen, C., Guerit, L., Foreman, B. Z., Hassenruck-Gudipati, H. J., Adatte, T., Honegger, L., Perret, M., Sluijs, A. and Castelltort, S.: Estimating regional flood discharge during Palaeocene-Eocene global warming, Sci. Rep., 8, 1–8, doi:10.1038/s41598-018-31076-3, 2018.

Clevis, Q., de Jager, G., Nijman, W. and de Boer, P. L.: Stratigraphic signatures of translation of thrust-sheet top basins over low-angle detachment faults, Basin Res., 16, 145–163, doi:10.1046/j.1365-2117.2003.00226.x, 2004.

Cramer, B. S., Wright, J. D., Kent, D. V. and Aubry, M. P.: Orbital climate forcing of δ13C excursions in the late Paleocene-early Eocene (chrons C24n-C25n), Paleoceanography, 18, 1–25, doi:10.1029/2003PA000909, 2003.

Croudace, I. W. and Rothwell, R. G.: Micro-XRF Studies of Sediment Cores, edited by I. W. Croudace and R. G. Rothwell, Springer Netherlands, Dordrecht., 2015.

Davidson, E. A. and Janssens, I. A.: Temperature sensitivity of soil carbon decomposition and feedbacks to climate change, Nature, 440, 165–173, doi:10.1038/nature04514, 2006.

Davidson, E. A., Trumbore, S. E., Amundson, R. and reply — Davidson, R.: Question the Validity of Our Conclusions on the Grounds That Differences in Disturbance, High Variability Among Sites, and the Use of a Single-Pool Model To Estimate Turnover, Nat. Nat. Nat. Biotropica Nat. Trumbore, S. E. Ecol. Appl.. A. Amundson, R. A. Sci. Chang. Biol. Nat. Sci., 48, 21–51, 2000.

Deconto, R. M., Galeotti, S., Pagani, M., Tracy, D., Schaefer, K., Zhang, T., Pollard, D. and Beerling, D. J.: Past extreme warming events linked to massive carbon release from thawing permafrost, Nature, 484, 87–91, doi:10.1038/nature10929, 2012.

Doetterl, S., Stevens, A., Six, J., Merckx, R., Van Oost, K., Casanova Pinto, M., Casanova-Katny, A., Muñoz, C., Boudin, M., Zagal Venegas, E. and Boeckx, P.: Soil carbon storage controlled by interactions between geochemistry and climate, Nat. Geosci., 8, 780–783, doi:10.1038/ngeo2516, 2015.

Duller, R. A., Armitage, J. J., Manners, H. R., Grimes, S. and Jones, T. D.: Delayed sedimentary response to abrupt climate change at the Paleocene-Eocene boundary, northern Spain, Geology, 47, 159–162, doi:10.1130/G45631.1, 2019.

Dunkley Jones, T., Manners, H. R., Hoggett, M., Turner, S. K., Westerhold, T., Leng, M. J., Pancost, R. D., Ridgwell, A., Alegret, L., Duller, R. and Grimes, S. T.: Dynamics of sediment flux to a bathyal continental margin section through the Paleocene-Eocene Thermal Maximum, Clim. Past, 14, 1035–1049, doi:10.5194/cp-14-1035-2018, 2018.

Farrell, S. G., Williams, G. D. and Atkinson, C. D.: Constraints on the age of movement of the Montsech and Cotiella Thrusts, south central Pyrenees, Spain, J. Geol. Soc. London., 144, 907–914, doi:10.1144/gsjgs.144.6.0907, 1987.

Foreman, B. Z. and Straub, K. M.: Autogenic geomorphic processes determine the resolution and fidelity of terrestrial paleoclimate records, Sci. Adv., 3, 1–12, doi:10.1126/sciadv.1700683, 2017.

Foreman, B. Z., Heller, P. L. and Clementz, M. T.: Fluvial response to abrupt global warming at the Palaeocene/Eocene boundary, Nature, 490, 92–95, doi:10.1038/nature11513, 2012.

Gallagher, T. M. and Sheldon, N. D.: Combining soil water balance and clumped isotopes to understand the nature and timing of pedogenic carbonate formation, Chem. Geol., doi:10.1016/j.chemgeo.2016.04.023, 2016.

Giusberti, L., Boscolo Galazzo, F. and Thomas, E.: Variability in climate and productivity during the Paleocene-Eocene Thermal Maximum in the western Tethys (Forada section), Clim. Past, 12, 213–240, doi:10.5194/cp-12-213-2016, 2016.

Hasiotis, S. T.: Reconnaissance of Upper Jurassic Morrison Formation ichnofossils, Rocky Mountain Region, USA: Paleoenvironmental, stratigraphic, and paleoclimatic significance of terrestrial and freshwater ichnocoenoses, Sediment. Geol., 167, 177–268, doi:10.1016/j.sedgeo.2004.01.006, 2004.

Hessler, A. M., Zhang, J., Covault, J. and Ambrose, W.: Continental weathering coupled to Paleogene climate changes in North America, Geology, 45, doi:10.1130/G39245.1, 2017.

Hunger, T.: Climatic signals in the Paleocene fluvial formation of the Tremp-Graus Basin, Pyrenees, Spain, MSc Thesis, Université de Genève, pp. 123, url:https://archive-ouverte.unige.ch/unige:124264., 2018.

Hyland, E. G. and Sheldon, N. D.: Coupled CO2-climate response during the Early Eocene Climatic Optimum, Palaeogeogr. Palaeoclimatol. Palaeoecol., 369, 125–135, doi:10.1016/j.palaeo.2012.10.011, 2013.

Kapellos, C. and Schaub, H.: Zur Korrelation von Biozonierungen mit Grossforaminiferen und Nannoplankton im Paläogen der Pyrenäen, Eclogae Geol. Helv., 66, 687–737, 1973.

Khozyem Saleh, H. M. A.: Sedimentology, geochemistry and mineralogy of the Paleocene-Eocene thermal maximum (PETM) : sediment records from Egypt, India and Spain. PhD Thesis, Université de Lausanne, url:https://serval.unil.ch/notice/serval:BIB_181B1630AE67., 2013.

Kirtland-Turner, S., Sexton, P. F., Charles, C. D. and Norris, R. D.: Persistence of carbon release events through the peak of early Eocene global warmth, Nat. Geosci., 7, 748–751, doi:10.1038/NGEO2240, 2014.

Klemmedson, J. O.: Soil organic matter in arid and semiarid ecosystems: Sources, accumulation, and distribution, Arid Soil Res. Rehabil., 3, 99–114, doi:10.1080/15324988909381194, 1989.

Koch, P. L., Zachos, J. C. and Gingerich, P. D.: Correlation between isotope records in marine and continental carbon reservoirs near the Palaeocene/Eocene boundary, Nature, 358, 319–322, doi:10.1038/358319a0, 1992.

Koch, P. L., Zachos, J. and Dettman, D. L.: Stable isotope stratigraphy and paleoclimatology of the Paleogene Bighorn Basin (Wyoming, USA), Palaeogeogr. Palaeoclimatol. Palaeoecol., 115, 61–89, doi:10.1016/0031-0182(94)00107-J, 1995.

Koch, P. L., Clyde, W. C., Hepple, R. P., Fogel, M. L., Wing, S. L. and Zachos, J. C.: Carbon and oxygen isotope records from Paleosols spanning the Paleocene-Eocene boundary, Bighorn Basin, Wyoming, Causes Consequences Glob. Warm Clim. Early Paleogene, 369, 49–64, doi:https://doi.org/10.1130/0-8137-2369-8.49, 2003.

Koven, C. D., Hugelius, G., Lawrence, D. M. and Wieder, W. R.: Higher climatological temperature sensitivity of soil carbon in cold than warm climates, Nat. Clim. Chang., 7, 817–822, doi:10.1038/nclimate3421, 2017.

Kraus, M. J. and Aslan, A.: Eocene hydromorphic paleosols: significance for interpreting ancient floodplain processes, J. Sediment. Res., 63, 453–463, doi:10.1306/D4267B22-2B26-11D7-8648000102C1865D, 1993.

Kraus, M. J. and Riggins, S.: Transient drying during the Paleocene-Eocene Thermal Maximum (PETM): Analysis of paleosols in the bighorn basin, Wyoming, Palaeogeogr. Palaeoclimatol. Palaeoecol., 245, 444–461, doi:10.1016/j.palaeo.2006.09.011, 2007.

Kraus, M. J., Woody, D. T., Smith, J. J. and Dukic, V.: Alluvial response to the Paleocene-Eocene Thermal Maximum climatic event, Polecat Bench, Wyoming (U.S.A.), Palaeogeogr. Palaeoclimatol. Palaeoecol., 435, 177–192, doi:10.1016/j.palaeo.2015.06.021, 2015.

Kukla, T., Winnick, M. J., Maher, K., Ibarra, D. E. and Chamberlain, C. P.: The Sensitivity of Terrestrial δ18O Gradients to Hydroclimate Evolution, J. Geophys. Res. Atmos., 124, 563–582, doi:10.1029/2018JD029571, 2019.

Lauretano, V., Littler, K., Polling, M., Zachos, J. C. and Lourens, L. J.: Frequency, magnitude and character of hyperthermal events at the onset of the Early Eocene Climatic Optimum, Clim. Past, 11, 1313–1324, doi:10.5194/cp-11-1313-2015, 2015.

Lauretano, V., Hilgen, F. J., Zachos, J. C. and Lourens, L. J.: Astronomically tuned age model for the early Eocene carbon isotope events: A new high-resolution δ13Cbenthic record of ODP Site 1263 between ~ 49 and ~ 54 Ma, Newsletters Stratigr., 49, 383–400, doi:10.1127/nos/2016/0077, 2016.

Lourens, L. J., Sluijs, A., Kroon, D., Zachos, J. C., Thomas, E., Röhl, U., Bowles, J. and Raffi, I.: Astronomical pacing of late Palaeocene to early Eocene global warming events, Nature, 435, 1083–1087, doi:10.1038/nature03814, 2005.

Lunt, D. J., Ridgwell, A., Sluijs, A., Zachos, J., Hunter, S. and Haywood, A.: A model for orbital pacing of methane hydrate destabilization during the Palaeogene, Nat. Geosci., 4, 775–778, doi:10.1038/ngeo1266, 2011.

Lupker, M., France-Lanord, C., Lavé, J., Bouchez, J., Galy, V., Métivier, F., Gaillardet, J., Lartiges, B. and Mugnier, J.-L.: A Rouse-based method to integrate the chemical composition of river sediments: Application to the Ganga basin, J. Geophys. Res., 116, F04012, doi:10.1029/2010JF001947, 2011.

Lupker, M., France-Lanord, C., Galy, V., Lavé, J., Gaillardet, J., Gajurel, A. P., Guilmette, C., Rahman, M., Singh, S. K. and Sinha, R.: Predominant floodplain over mountain weathering of Himalayan sediments (Ganga basin), Geochim. Cosmochim. Acta, 84, 410–432, doi:10.1016/j.gca.2012.02.001, 2012.

Marriott, S. B. and Wright, V. P.: Palaeosols as indicators of geomorphic stability in two Old Red Sandstone alluvial suites, South Wales, J. Geol. Soc. London., 150, 1109–1120, doi:10.1144/gsjgs.150.6.1109, 1993.

Marzo, M., Nijman, W. and Puigdefàbregas, C.: Architecture of the Castissent fluvial sheet sandstones, Eocene, South Pyrenees, Spain, Sedimentology, 35, 719–738, doi:10.1111/j.1365-3091.1988.tb01247.x, 1988.

McInerney, F. A. and Wing, S. L.: The Paleocene-Eocene Thermal Maximum: A Perturbation of Carbon Cycle, Climate, and Biosphere with Implications for the Future, Annu. Rev. Earth Planet. Sci., 39, 489–516, doi:10.1146/annurev-earth-040610-133431, 2011.

Melillo, J. M., Steudler, P. A., Aber, J. D. M., Newkirk, K., Lux, H., Bowles, F. P., Catricala, C., Magill, A., Ahrens, T. and Morrisseau, S.: Soil warming and carbon-cycle feedbacks to the climate system, Science, 298, 2173–2176, doi:10.2172/1129843, 2014.

Milliere, L., Hasinger, O., Bindschedler, S., Cailleau, G., Spangenberg, J. E. and Verrecchia, E. P.: Stable carbon and oxygen isotope signatures of pedogenic needle fibre calcite, Geoderma, 161, 74–87, doi:10.1016/j.geoderma.2010.12.009, 2011.

Millière, L., Spangenberg, J. E., Bindschedlera, S., Cailleaua, G. and Verrecchiaa, E. P.: Reliability of stable carbon and oxygen isotope compositions of pedogenic needle fibre calcite as environmental indicators: Examples from Western Europe, Isotopes Environ. Health Stud., 47, 341–358, doi:10.1080/10256016.2011.601305, 2011.

Mutti, E., Séguret, M. and Sgavetti, M.: Sedimentation and Deformation in the Tertiary Sequences of the Southern Pyrenees., 1988.

Nicolaides, E.: Analyses des sédiments marins et continentaux éocènes dans les Pyrénées Espagnoles, BSc Thesis, Université de Lausanne., 2017.

Nicolo, M. J., Dickens, G. R., Hollis, C. J. and Zachos, J. C.: Multiple early Eocene hyperthermals: Their sedimentary expression on the New Zealand continental margin and in the deep sea, Geology, 35, 699, doi:10.1130/G23648A.1, 2007.

Nijman, W.: Cyclicity and basin axis shift in a piggyback basin: towards modelling of the Eocene Tremp-Ager Basin, South Pyrenees, Spain, Geol. Soc. London, Spec. Publ., 134, 135–162, doi:10.1144/GSL.SP.1998.134.01.07, 1998.

Nijman, W. and Nio, S.-D.: The Eocene Montañana Delta, 1975.

Nijman, W. and Puigdefabregas, C.: Coarse-grained point bar structure in a molasse-type fluvial system, Eocene Castisent sandstone Formation, south Pyrenean Basin., Fluv. Sedimentol. Can Soc Pet. Geol Mem 5, 5, 487–510, 1978.

Paillard, D., Labeyrie, L. and Yiou, P.: Macintosh Program performs time-series analysis, Eos, Trans. Am. Geophys. Union, 77, 379–379, doi:10.1029/96eo00259, 1996.

Payros, A., Tosquella, J., Bernaola, G., Dinarès-Turell, J., Orue-Etxebarria, X. and Pujalte, V.: Filling the North European Early/Middle Eocene (Ypresian/Lutetian) boundary gap: Insights from the Pyrenean continental to deep-marine record, Palaeogeogr. Palaeoclimatol. Palaeoecol., 280, 313–332, doi:10.1016/j.palaeo.2009.06.018, 2009.

Payros, A., Ortiz, S., Millán, I., Arostegi, J., Orue-Etxebarria, X. and Apellaniz, E.: Early Eocene climatic optimum: Environmental impact on the North Iberian continental margin, Bull. Geol. Soc. Am., 127, 1632–1644, doi:10.1130/B31278.1, 2015.

Pickering, K. T. and Bayliss, N. J.: Deconvolving tectono-climatic signals in deep-marine siliciclastics, Eocene Ainsa basin, Spanish Pyrenees: Seesaw tectonics versus eustasy, Geology, 37, 203–206, doi:10.1130/G25261A.1, 2009.

Poyatos-Moré, M.: Physical Stratigraphy and Facies Analysis of the Castissent Tecto-Sedimentary Unit, PhD Thesis, Universidad Autónoma de Barcelona, pp. 284, url:https://ddd.uab.cat/record/127119., 2014.

Prochnow, S. J., Nordt, L. C., Atchley, S. C. and Hudec, M. R.: Multi-proxy paleosol evidence for middle and late Triassic climate trends in eastern Utah, Palaeogeogr. Palaeoclimatol. Palaeoecol., 232, 53–72, doi:10.1016/j.palaeo.2005.08.011, 2006.

Puigdefabregas, C., Souquet, P., Puigdefàbregas, C. and Souquet, P.: Tecto-sedimentary cycles and depositional sequences of the mesozoic and tertiary from the pyrenees, Tectonophysics, 129, 173–203, doi:10.1016/0040-1951(86)90251-9, 1986.

Pujalte, V., Baceta, J. I. and Schmitz, B.: A massive input of coarse-grained siliciclastics in the Pyrenean Basin during the PETM: The missing ingredient in a coeval abrupt change in hydrological regime, Clim. Past, 11, 1653–1672, doi:10.5194/cp-11-1653-2015, 2015.

Raich, J. and Schlesinger, W.: The global carbon dioxide flux in soil respiration, Tellus, 44 B, 81–99, 1992.

Retallack, G. J.: The environmental factor approach to the interpretation of paleosols, Factors soil Form. Proc. Symp. Denver, 1991, 33, 31–64, 1994.

Romans, B. W., Castelltort, S., Covault, J. A., Fildani, A. and Walsh, J. P. P.: Environmental signal propagation in sedimentary systems across timescales, Earth-Science Rev., 153, 7–29, doi:10.1016/j.earscirev.2015.07.012, 2016.

Schaub, H.: Über die Grossforaminiferen im Untereocaen von Campo (Ober-Aragonien), Eclogae Geol. Helv., 59, 355–391, 1966.

Schaub, H.: Nummulites et Assilines de la Téthys paléogène. Taxonomie, phylogenèse et biostratigraphie, Mémoires suisses de Paléontologie, 104, 236 p., 1981.

Schlunegger, F. and Castelltort, S.: Immediate and delayed signal of slab breakoff in Oligo/Miocene Molasse deposits from the European Alps, Sci. Rep., 6, doi:10.1038/srep31010, 2016.

Schmitz, B. and Pujalte, V.: Sea-level, humidity, and land-erosion records across the initial Eocene thermal maximum from a continental-marine transect in northern Spain, Geology, 31, 689–692, doi:10.1130/G19527.1, 2003.

Schmitz, B., Pujalte, V. and Núñez-Betelu, K.: Climate and sea-level perturbations during the Initial Eocene Thermal Maximum: Evidence from siliciclastic units in the Basque basin (Ermua, Zumaia and Trabakua Pass), northern Spain, Palaeogeogr. Palaeoclimatol. Palaeoecol., 165, 299–320, doi:10.1016/S0031-0182(00)00167-X, 2001.

Seeland, D.: Late Cretaceous , Paleocene , and Early Eocene Paleogeography of the Bighorn Basin and Northwestern Wyoming, Cretac. Low. Tert. Rocks Bighorn Basin, Wyoming Mont. 49th Annu. F. Conf. Guideb., 1–29, 1998.

Sexton, P. F., Norris, R. D., Wilson, P. A., Pälike, H., Westerhold, T., Röhl, U., Bolton, C. T. and Gibbs, S.: Eocene global warming events driven by ventilation of oceanic dissolved organic carbon, Nature, 471, 349–

353, doi:10.1038/nature09826, 2011.

Sheldon, N. D. and Tabor, N. J.: Quantitative paleoenvironmental and paleoclimatic reconstruction using paleosols, Earth-Science Rev., 95, 1–52, doi:10.1016/j.earscirev.2009.03.004, 2009.

Sheldon, N. D., Retallack, G. J. and Tanaka, S.: Geochemical Climofunctions from North American Soils and Application to Paleosols across the Eocene-Oligocene Boundary in Oregon, J. Geol., 110, 687–696, doi:10.1086/342865, 2002.

Slessarev, E. W., Lin, Y., Bingham, N. L., Johnson, J. E., Dai, Y., Schimel, J. P. and Chadwick, O. A.: Water balance creates a threshold in soil pH at the global scale, Nature, 540, 567–569, doi:10.1038/nature20139, 2016.

Slotnick, B. S., Dickens, G. R., Nicolo, M. J., Hollis, C. J., Crampton, J. S., Zachos, J. C. and Sluijs, A.: Large-Amplitude Variations in Carbon Cycling and Terrestrial Weathering during the Latest Paleocene and Earliest Eocene: The Record at Mead Stream, New Zealand, J. Geol., 120, 487–505, doi:10.1086/666743, 2012.

Sluijs, A. and Dickens, G. R.: Assessing offsets between the δ13C of sedimentary components and the global exogenic carbon pool across early Paleogene carbon cycle perturbations, Global Biogeochem. Cycles, 26, 1–14, doi:10.1029/2011GB004224, 2012.

Soler, L. C.: Revisión del género Diacodexis (Artiodactyla, Mammalia) en el Eoceno inferior del Noreste de España, Geobios, 37, 325–335, doi:10.1016/j.geobios.2004.03.001, 2004.

Stap, L., Lourens, L. J., Thomas, E., Sluijs, A., Bohaty, S. and Zachos, J. C.: High-resolution deep-sea carbon and oxygen isotope records of Eocene Thermal Maximum 2 and H2, Geology, 38, 607–610, doi:10.1130/G30777.1, 2010.

Straub, K. M. and Foreman, B. Z.: Geomorphic stasis and spatiotemporal scales of stratigraphic completeness, Geology, 46, 311–314, doi:10.1130/G40045.1, 2018.

Teixell, A.: Crustal structure and orogenic material budget in the west central Pyrenees, Tectonics, 17, 395–406, doi:10.1029/98TC00561, 1998.

Torn, M. S., Trumbore, S. E., Chadwick, O. A., Vitousek, P. M. and Hendricks, D. M.: Mineral control of soil organic carbon storage and turnover, Nature, 389, 170–173, doi:10.1038/38260, 1997.

Tosquella, J.: Els Nummulitinae del Paleocè-Eocè inferior de la conca sudpirinenca, Unpublished PhD Thesis, Universitat de Barcelona., 1995.

Tosquella, J., Serra-Kiel, J., Ferràndez, C. and Samsó, J. M.: Las biozonas de nummulitidos del Paleoceno Superior-Eoceno Inferior de la Cuenca Pirenaica, Acta Geol. Hisp., 31, 23–36, 1998.

Trampush, S. M., Hajek, E. A., Straub, K. M. and Chamberlin, E. P.: Identifying autogenic sedimentation in fluvial-deltaic stratigraphy: Evaluating the effect of outcrop-quality data on the compensation statistic, J. Geophys. Res. Earth Surf., 122, 91–113, doi:10.1002/2016JF004067, 2017.

Trumbore, S. E., Chadwick, O. A. and Amundson, R.: Rapid exchange between soil carbon and atmospheric carbon dioxide driven by temperature change, Science, 272, 393–396, doi:10.1126/science.272.5260.393, 1996.

Turner, J. N., Jones, A. F., Brewer, P. A., Macklin, M. G. and Rassner, S. M.: Micro-XRF Applications in Fluvial Sedimentary Environments of Britain and Ireland: Progress and Prospects, in In Micro-XRF Studies of Sediment Cores, pp. 227–265, Springer, Dordrecht., 2015.

Wang, Y., Straub, K. M. and Hajek, E. a.: Scale-dependent compensational stacking: An estimate of autogenic time scales in channelized sedimentary deposits, Geology, 39, 811–814, doi:10.1130/G32068.1, 2011.

Westerhold, T. and Röhl, U.: High resolution cyclostratigraphy of the early Eocene - New insights into the origin of the Cenozoic cooling trend, Clim. Past, 5, 309–327, doi:10.5194/cp-5-309-2009, 2009.

Westerhold, T., Röhl, U., Frederichs, T., Agnini, C., Raffi, I., Zachos, J. C. and Wilkens, R. H.: Astronomical calibration of the Ypresian timescale: Implications for seafloor spreading rates and the chaotic behavior of the solar system?, Clim. Past, 13, 1129–1152, doi:10.5194/cp-13-1129-2017, 2017.

Westerhold, T., Röhl, U., Donner, B. and Zachos, J. C.: Global Extent of Early Eocene Hyperthermal Events: A New Pacific Benthic Foraminiferal Isotope Record From Shatsky Rise (ODP Site 1209), Paleoceanogr. Paleoclimatology, 33, 626–642, doi:10.1029/2017PA003306, 2018.

Whitchurch, a. L., Carter, A., Sinclair, H. D., Duller, R. a., Whittaker, a. C. and Allen, P. a.: Sediment routing system evolution within a diachronously uplifting orogen: Insights from detrital zircon thermochronological analyses from the South-Central Pyrenees, Am. J. Sci., 311, 442–482, doi:10.2475/05.2011.03, 2011.

Winnick, M. J., Caves, J. K. and Chamberlain, C. P.: A mechanistic analysis of early Eocene latitudinal gradients of isotopes in precipitation, Geophys. Res. Lett., 42, 8216–8224, doi:10.1002/2015GL064829, 2015.

Zachos, J., Pagani, H., Sloan, L., Thomas, E. and Billups, K.: Trends, rhythms, and aberrations in global climate 65 Ma to present, Science, 292, 686–693, doi:10.1126/science.1059412, 2001.

Zachos, J., Dickens, G. and Zeebe, R.: An early Cenozoic perspective on greenhouse warming and carbon-cycle dynamics., Nature, 451, 279–83, doi:10.1038/nature06588, 2008.

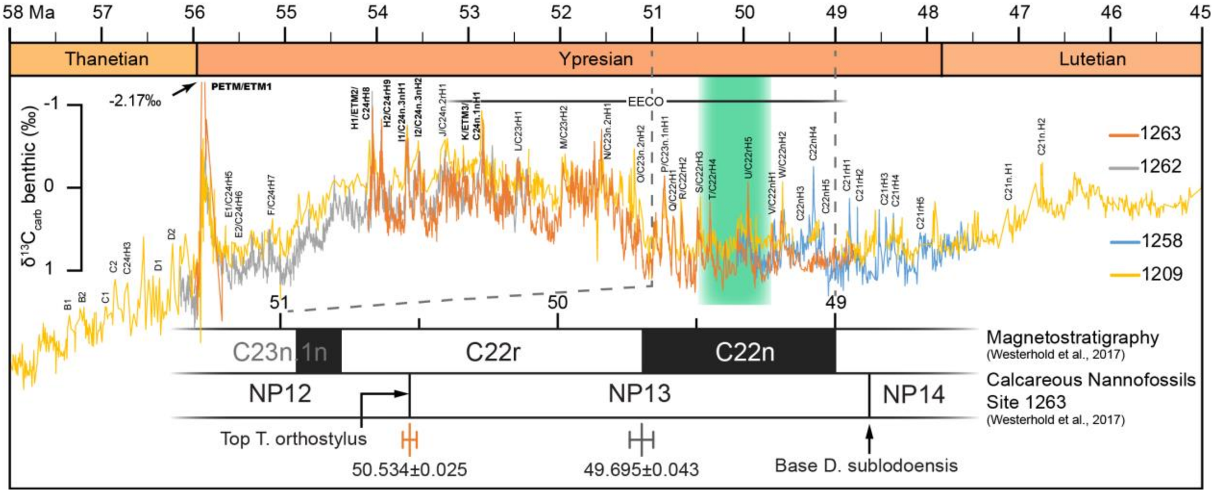

Figure 1: Late Paleocene and early-Eocene benthic carbon isotope record from Sites 1209, 1258, 1262 and 1263. Top of Chron C22r and top of T. orthostylus zone from site 1263 from Westerhold et al. (2017). Hyperthermal nomenclature from Cramer et al. (2003), Lauretano et al. (2016) and Westerhold et al. (2017). Castissent Fm. extension in green.

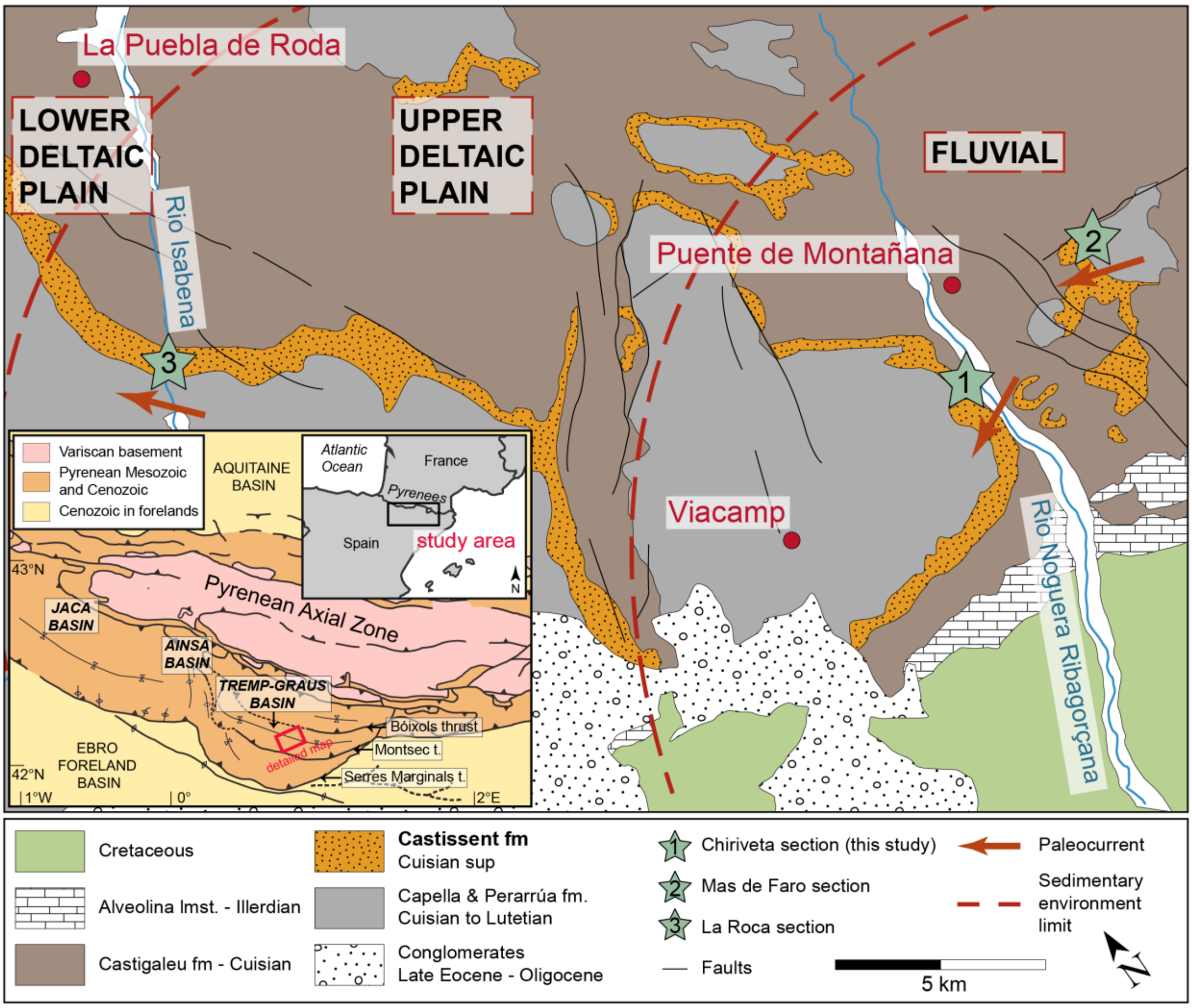

Figure 2: Simplified situation and geological map of the study area with main depositional paleo-environments (e.g., Nijman, 1998). The Castissent Fm. is a prominent fluvial unit particularly well-exposed in the Noguera Ribagorçana and Isabena river valleys. (1) Chiriveta section (2) Mas de Faro (3) La Roca section. Main paleoflow directions indicated in orange (from Nijman and Puigdefabregas, 1978). Regional map after Teixell (1998).

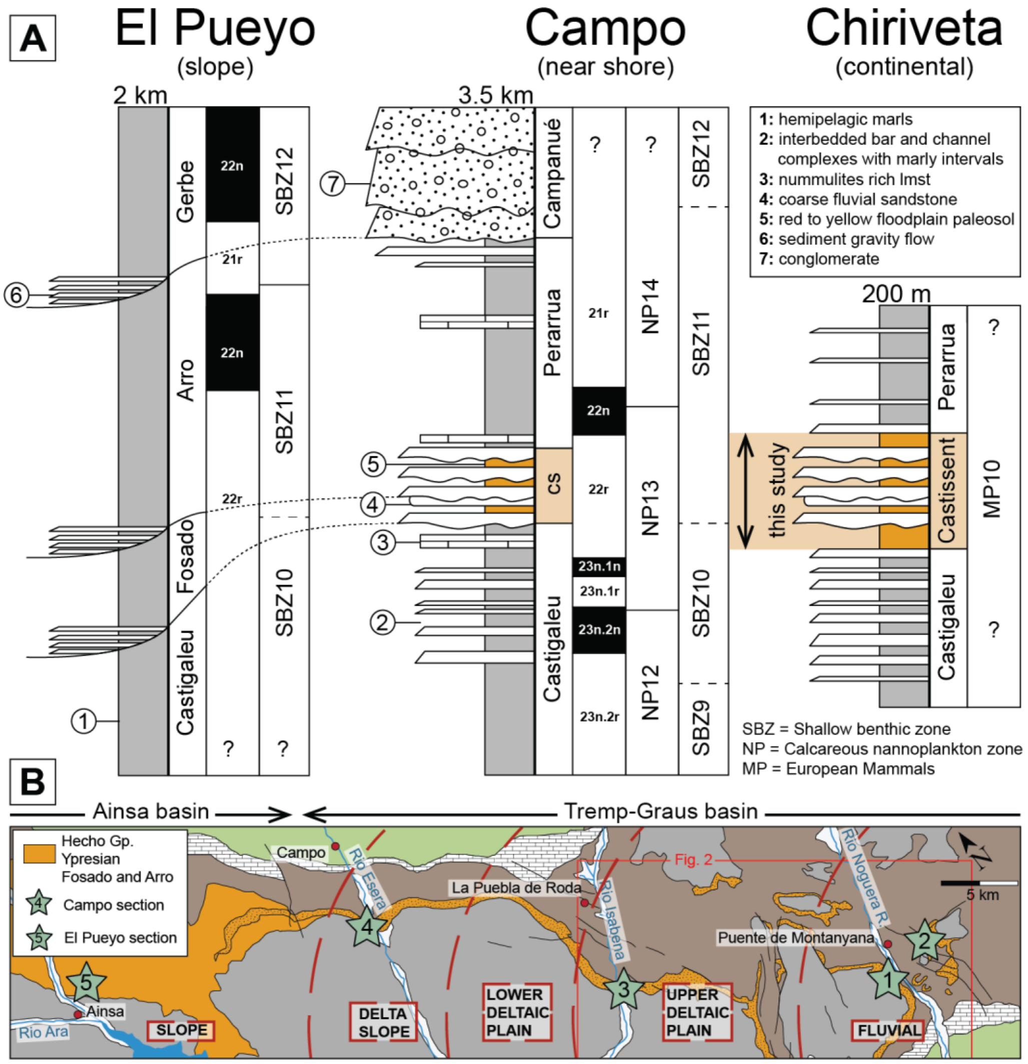

Figure 3: A - Time constraints on the Castissent Fm. MP zone from the continental section from Checa-Soler (2004) and Payros and Tosquella (2009). SBZ and NP in the Campo section from (Schaub, 1966, 1981; Kapellos and Schaub, 1973; Tosquella, 1995), magnetostratigraphy from Bentham and Burbank (1996). SBZ in El Pueyo section from Payros and Tosquella (2009). Magnetostratigraphy in El Pueyo from Poyatos-Moré (2014). B – Extended map of the study area. For map legend and references, see Fig. 2.

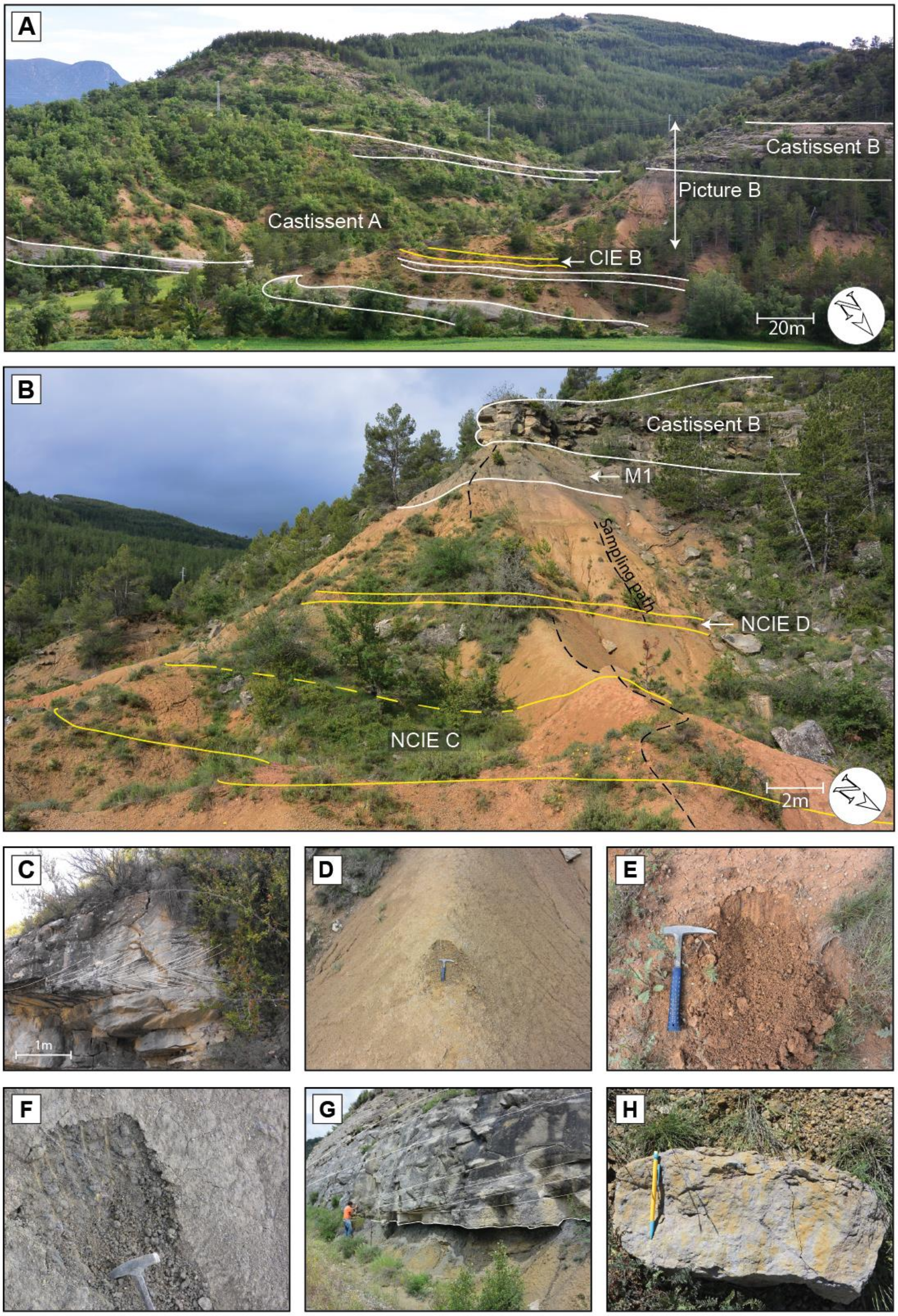

Figure 4: Field images of the Chiriveta section (42°7'56.57"N, 0°41'19.45"E). A – Outcrop view of Members A and B of the Castissent Formation. B – Close-up view of the upper part of Castissent A Member. Fluvial channel-fill deposits, intercalated in reddish floodplain and overbank deposits and regional marine incursions (M1). C – M0, first marine incursion at the base of the Castissent Fm. described by Marzo et al. (1988) expressed in the Chiriveta section by a tidal-influenced coarse sandstone with herringbone cross-stratification. D – Yellow mottled paleosol between CIE C and D. E – Redfloodplain interval equivalent of the CIE C. F – 2 m-thick grey interval interpreted as poorly drained brackish water facies and equivalent to the marine incursion M1. G – ~6m thick laterally extensive Castissent B sandbody incised in the underlying floodplain deposits. H – Mottled silt, interpreted as pedogenetic fluvial channel overbank deposits.

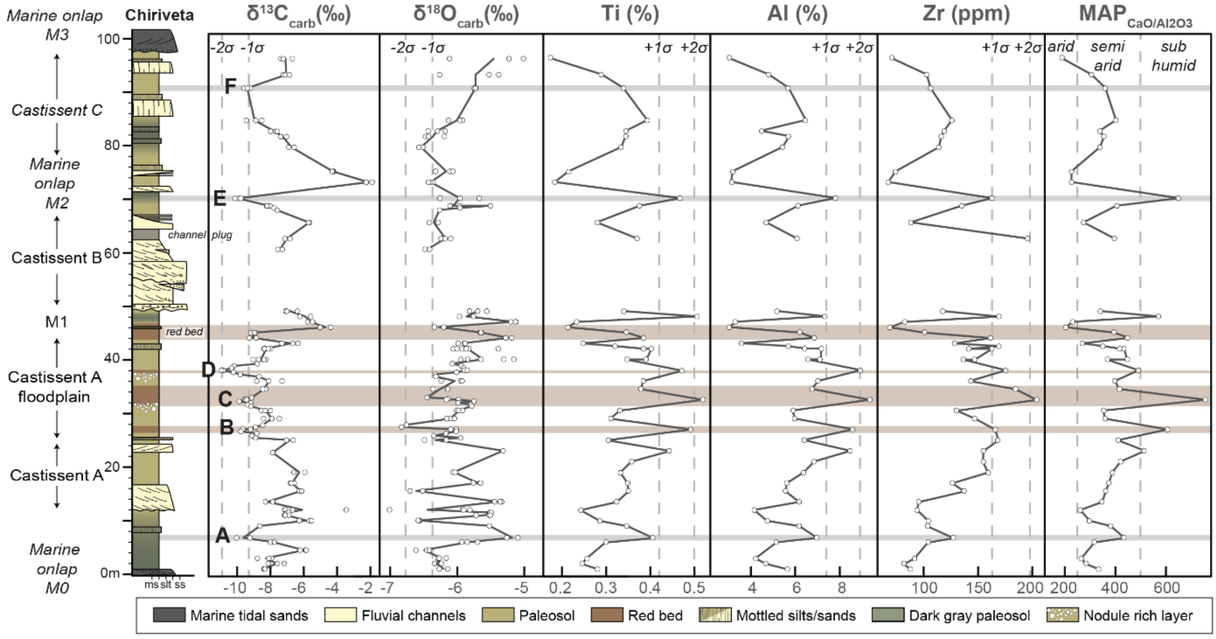

Figure 5: Isotopic and geochemical data from the Chiriveta section. For the isotope dataset, the curves passes through the mean values at each sample position. Samples with minimum in δ^{13}C values below 1 and 2 standard deviation are labelled A to F. Mean Annual Precipitation (MAP) was estimated from the empirical relationship between MAP and CaO to Al_2O_3 ratio (Sheldon et al., 2002).

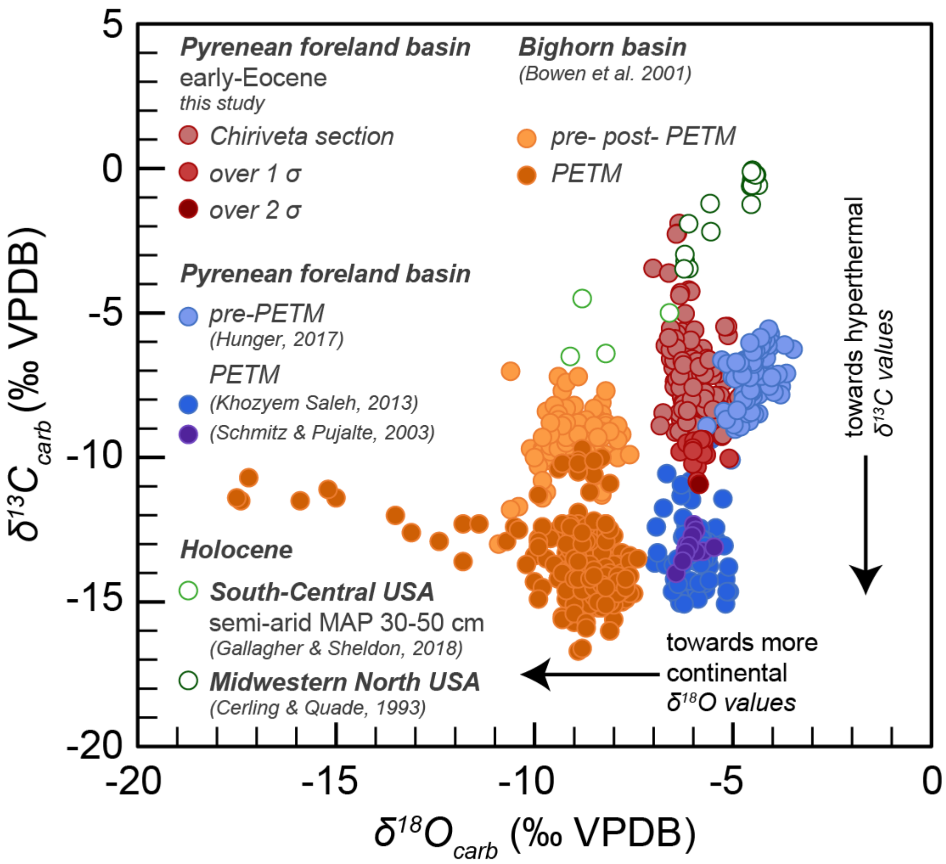

Figure 6: Continental δ^{13}C and δ^{18}O values from the early Eocene Castissent Fm. in the Chiriveta section (this study) plotted with pre- and syn-PETM δ^{13}C and δ^{18}O values from the same area (Khozyem Saleh, 2013; Hunger, 2018) and Pre-, syn and post-PETM values from the Bighorn Basin (Bowen et al., 2001) as well as recent pedogenic carbonate isotopic values (Cerling and Quade, 1993; Gallagher and Sheldon, 2016).

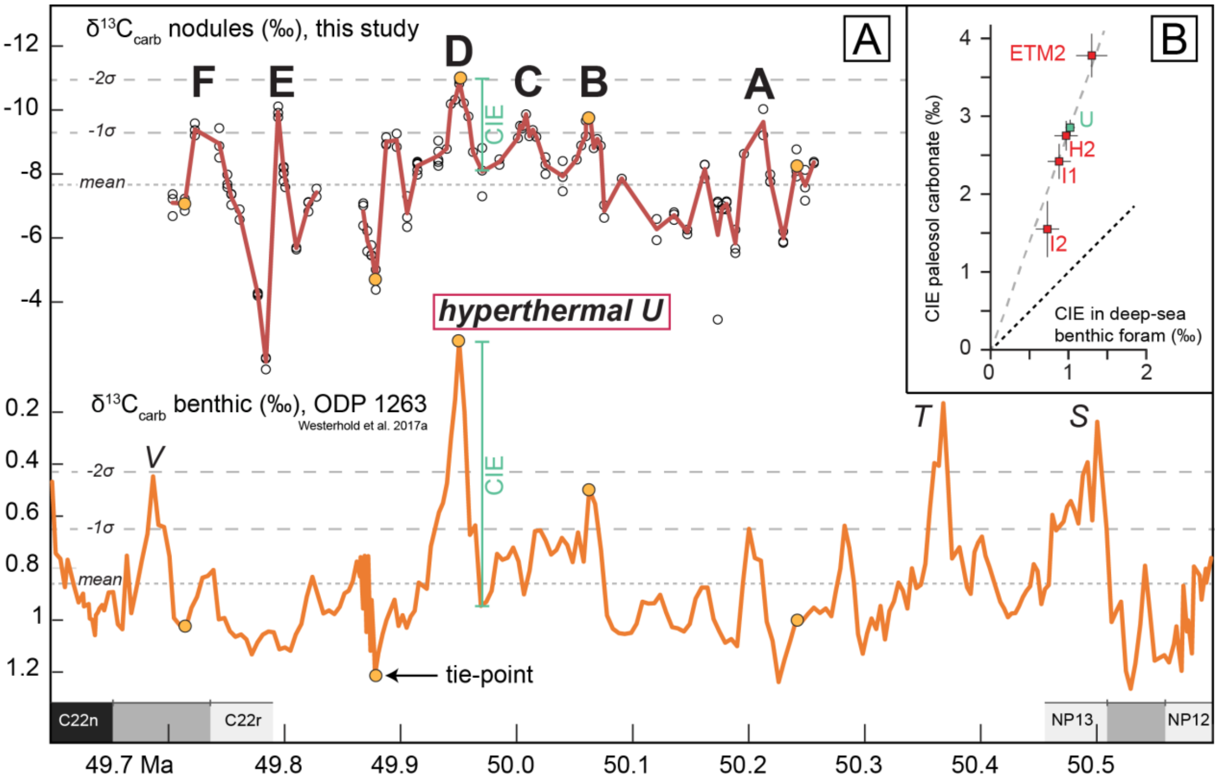

Figure 7: A - Scaling of the Chiriveta isotopic section with the time equivalent interval of site 1263 (Westerhold et al., 2017). The correlation was calculated using the Analyseries software (Paillard et al., 1996) and centred on CIE D and hyperthermal U. Mean, minus 1 and 2 SD lines on the global record were calculated sets over the selected time period. The correlation coefficient (*r*) between the two curves is 0.65. B - Hyperthermal U amplitude in paleosol carbonate and benthic foraminifera (inset B after Abels et al. (2016))

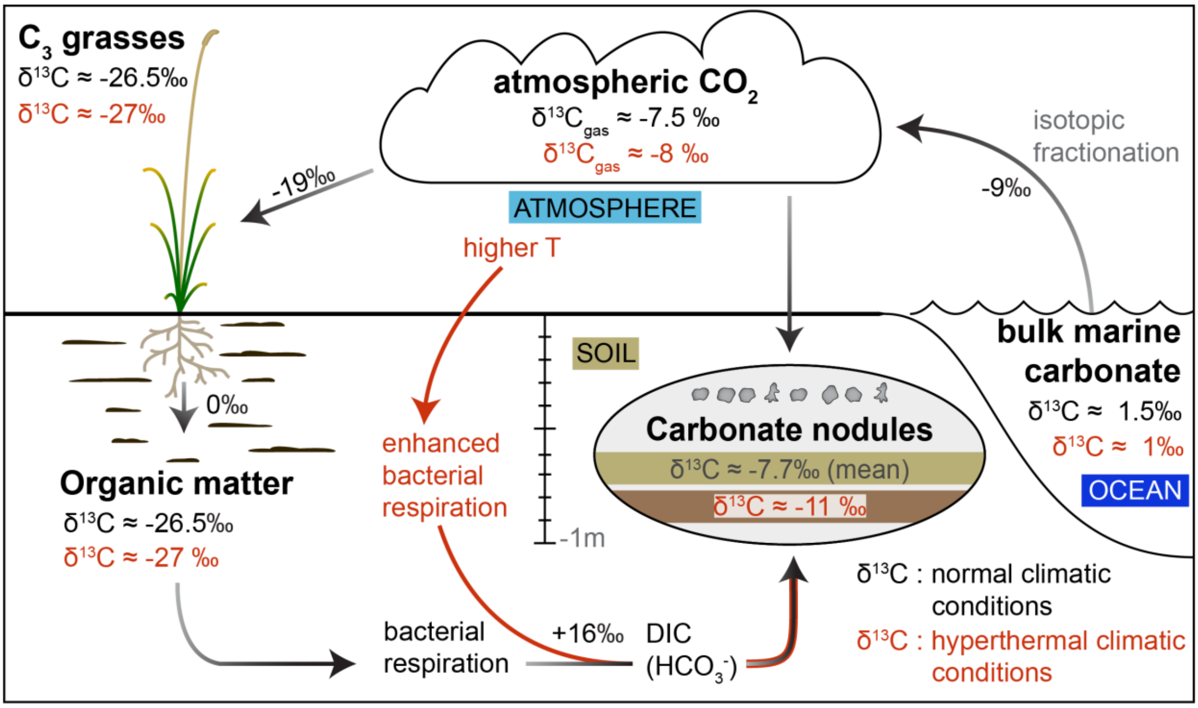

Figure 8: Components influencing the δ^{13}C values of pedogenic carbonate nodules. Mean early Eocene bulk marine carbonate and small scale hyperthermal (all except PETM) are from Westerhold et al. (2018). Fractionation value between organic matter and carbonate nodules are based on Sheldon and Tabor (2009). All other fractionation values are based on Koch et al. (1995). Mean carbonate nodule values come from this study.